AIAA SciTech
13-17 January 2014, National Harbor, Maryland
52nd Aerospace Sciences Meeting

Pitching Airfoil Performance Enhancement Using Co-Flow Jet Flow Control at High Mach Number

Alexis Lefebvre*, G.-C. Zha†
Dept. of Mechanical and Aerospace Engineering
University of Miami
Coral Gables, Florida 33124
E-mail: gzha@miami.edu

Abstract

Pitching airfoils with Co-Flow Jet (CFJ) flow control are simulated using Unsteady Reynolds Average Navier-Stokes (URANS) at Mach number 0.4 with reduced frequency of 0.1. The flow is transonic with shock wave boundary layer interaction. A 5th order WENO scheme for the inviscid flux, a 4th order central differencing model for the viscous terms and the one equation Spalart-Allmaras model for the turbulence are used to resolve the flow. The airfoil oscillate around its mean AoA of 10° with amplitude of 5°, 7.5° and 10°. The study demonstrates that the CFJ pitching airfoil is very effective to remove dynamic stall at high Mach number of 0.4. The performance is significantly enhanced with radically increased lift, reduced drag, and decreased moment variation.

Nomenclature

CFJ	Co-flow jet
AoA	Angle of attack
LE	Leading edge
TE	Trailing edge
BL	Boundary layer
$ZNMF$	Zero-net mass-flux
M	Mach number
α_0	Mean angle of attack
α_1	Amplitude of oscillation
ω	Angular velocity of oscillation
S	Planform area
c	Profile chord
ρ	Air density
U	Flow velocity
q	Dynamic pressure $0.5\,\rho\,U^2$
p	Static pressure
$\dot{m}$	Mass flow
∞	Free stream conditions
$_j$	Jet conditions
k	Reduced frequency $\omega\,c/(2\,U_\infty)$
τ	Dimensionless time $2\,t\,U_\infty/c$

* Graduate Student, AIAA Member
† Professor, AIAA Associate Fellow

t	Real time
C_L	Lift coefficient $L/(q_\infty S)$
C_D	Drag coefficient $D/(q_\infty S)$
C_p	Pressure coefficient $(p - p_\infty)/q$
C_μ	Jet momentum coef. $\dot{m}_j U_j/(q S)$

1 Introduction

1.1 State of the Art Overview

The forward moving helicopter blades undergo a sinusoidal movement in order to achieve the balance of lift between advancing and retreating side of the rotor disk. The angle of attack (AoA) is minimum for the advancing blade while the retreating blade must increase the AoA in order to balance the lift.

The physics of the dynamic stall is well documented by Bousman [1] in his study including a level flight case at high altitude, a diving turn at high load factor, and the UTTAS pull-up maneuver. The dynamic stall is much alike for all of these flight conditions characterized by the shedding of a vortex at a near leading edge (LE) position both in simulation and in two-dimensional wind tunnel testing. Similar observation are obtained by McCroskey et al. [2] who conclude that dynamic stall come from the breakdown of a turbulent boundary layer (BL) as opposed to the burst of a laminar separation bubble. As the dynamic vortex is initiated, the blade experiences a peak performance in term of lift, drag and moment. However, as the vortex structures move downward, the performance collapses and results in a hysteresis loop behavior for forces and moment. The sudden nose-down moment peak submits the blade to large torsion that leads to fatigue and structure failure [3], and severely impairs the maneuverability of the rotorcraft [1].

In order to extend the flight envelop of rotor craft, research has been done to mitigate the dynamic stall. Early studies show that modifying the airfoil profile alone [4, 5] could improve slightly the performance during a light stall but have limited effect on the deep stall. This suggests that more radical solution have to be found to remove the dynamic stall. One of the method is to introduce slat in the blade design. McAlister et al. [6] studied experimentally the VR-7 slatted airfoil for a range of AoA. The slat configuration is able to minimize the lift collapse due to dynamic stall and to effectively smooth the moment coefficient. Reynolds number shows little influence on the slat effect. However the slatted configuration is found to have only moderate increase in average L/D over the cycle and maximum drag reaches a value well above 0.3 at large AoA.

In a more recent study Mishra [7] shows the effect of two slats configurations on the dynamic stall of the rotor blade UH60A. His results confirm the static slat effectiveness in reducing forces hysteresis during dynamic stall and smoothing the moment coefficient. Dynamic slats are not found to generate better results than the static slat configuration.

Yee et al. [8] studied the aerodynamic characteristics of the Gurney flap using 2D simulation for various Mach number and flap height. They found that a 2% height Gurney flap increases the effective camber and nose-down moment of the airfoil. The performance is slightly increased in the light stall but no substantial improvement is found for the deep stall case.

Thakkar et al. [9] explored a new single-crystal piezoceramic for its potential to torsionally actuate the elastic rotor blade utilizing the induced shear mechanism of piezoceramics. Their numerical study shows a possible reduction of the AoA by up to 8.7°, which suggests the possibility to dynamically twist the blade to suppress the dynamic stall. However performance improvements are yet to be quantified.

Another promising study have been done by Sun et al. [10] in their numerical study of tangential jet effect on dynamic stall using RANS equations using Baldwin-Lomax turbulence model. Their study

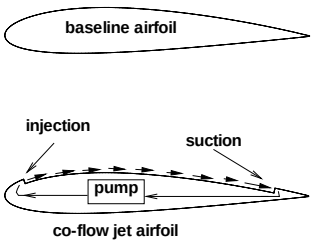

Figure 1: CFJ airfoil concept

focused on a pitching motion of a NACA0012 with oscillating with 10° amplitude about a 15° mean angle at a reduced frequency in the range 0.15-0.25. They were able to mitigate the stall at $C_\mu = 0.7$ using steady jets. They also found that using unsteady jets with strength periodically varying with the wing cycle is more effective at reducing the dynamic stall. Also jet position at about 0.6% chord location is found to be more effective than a more downstream position. However their results are more qualitative than quantitative due to the lack of precision when resolving large separated flow. In addition, the injection only flow control has significantly higher equivalent drag [11]. $C_\mu = 0.7$ with injection only will bring excessive power consumption.

1.2 Co-Flow Jet (CFJ) Flow Control Airfoil

Recently, a zero-net mass-flux (ZNMF) co-flow jet flow control airfoil developed by Zha et al. [12, 11, 13, 14, 15, 16, 17] based on fluidic actuators is demonstrated to achieve radical lift augmentation, stall margin increase, and drag reduction for stationary airfoil due to its high control authority.

In the CFJ airfoil concept [11, 12, 13, 14, 15, 16, 17], an injection slot near leading edge (LE) and a suction slot near trailing edge (TE) on the airfoil suction surface are created as sketched in Fig. 1. A small amount of mass flow is withdrawn into the airfoil near the TE, pressurized and energized by a pumping system inside the airfoil, and then injected near the LE in the direction tangent to the main flow. The whole process does not add any mass flow to the system and hence is a ZNMF flow control. The energy expenditure is low [11, 17].

The goal of CFJ pitching airfoil is to remove dynamic stall in the typical pitching airfoil working range with drastic enhancement of maximum lift, drag reduction, and moment variation mitigation. A low moment variation during the pitching cycle leads to a better pitching control, a greater blade life expectancy, a reduced rotor vibration and lower noise [18]. The previous CFJ pitching airfoil study [19] at Mach number of 0.3 demonstrates a significant enhancement of pitching airfoil performance by removing the dynamic stall. However, the flow field of pitching airfoil at Mach 0.3 does not generates a strong shock and the flow field is generally benign. The purpose of this paper is to quantify the effects of CFJ on pitching airfoil at high Mach number of 0.4, at which strong shock-boundary layer interaction is unavoidable and makes flow control of pitching airfoil more difficult.

2 Numerical Simulations Overview

2.1 CFD Code

The FASIP (Flow-Acoustics-Structure Interaction Package) CFD code is used to conduct the numerical simulation. The 2D Reynolds averaged Navier-Stokes (RANS) equations with one-equation Spalart-Allmaras [20] turbulence model is used. A 5th order WENO scheme for the inviscid flux [21, 22, 23, 24, 25, 26, 27] and a 4th order central differencing for the viscous terms [21, 26] are employed to discretize the Navier-Stokes equations. The low diffusion E-CUSP scheme used as the approximate Riemann solver suggested by Zha et al [22] is utilized with the WENO scheme to evaluate the inviscid fluxes. Implicit time marching method using Gauss-Seidel line relaxation is used to achieve fast convergence rate[28]. Parallel computing is implemented to save wall clock simulation time[29]. The RANS solver is validated for CFJ static airfoil simulation [15].

2.2 Mesh

The computation mesh is constructed using the O-mesh topology in order to achieve high quality around the airfoil. The CFJ SC1095 airfoil mesh displayed Fig. 2 uses a total of 360 points around the airfoil partitioned into 240 points on suction surface and 120 points on the pressure surface, 180 points in the direction normal to the airfoil with an additional 50 points across the jet. Total mesh size is 77,800 cells, partitioned into 23 blocks for parallel computation. The farfield boundary is located 50 chords away from the airfoil. To resolve the turbulent boundary layer, the first grid point is placed at $y^+ \approx 0.75$. The baseline airfoil mesh with no flow control is constructed using the same strategy. The total baseline airfoil mesh size is 54,000 cells with 271 points around the airfoil and 181 points normal to the airfoil. The baseline airfoil mesh is split into 27 blocks for the parallel computing. For both baseline airfoil and CFJ airfoil, a refined grid is constructed using 50% more points in every direction and $y^+ \approx 0.50$.

2.3 Boundary Conditions

The wall treatment suggested in [25] to achieve the flux conservation on the wall is employed. The 3rd order accuracy no slip condition is enforced on the solid surface as described in [25]. Total pressure, total temperature and flow angle are specified as the inlet boundary conditions for the upstream portion of the farfield boundary and inside the injection cavity. Constant static pressure is used downstream at the farfield boundary and in the suction cavity.

To achieve zero-net mass-flux with the CFJ flow control, the injection mass flow must be equal to the mass flow entering the suction slot. Additionally, the jet strength must be controlled in order to reach the prescribed C_μ. This is achieved by iterating the jet total pressure until the C_μ value is within 1% of the prescribed value. At the suction cavity, the suction mass flow is matched to the injection mass flow by iterating the static pressure at the suction cavity. The process is iterated throughout the simulation until the specified moment coefficient is achieved and the injection and suction mass flow match.

2.4 Airfoil Configurations

The baseline SC1095 airfoil used on the UH-60 Black Hawk US-army helicopter is chosen due to the existence of experimental data from NASA [5] at M=0.3. Those experimental data were validated in out previous paper [19]. SC1095 CFJ pitching airfoil performs well at M=0.3. However the performance is decreased at M=0.4 due to a prominent LE stall that is difficult to remove with CFJ. This motivates to create a better CFJ airfoil for M=0.4. For this purpose we generated 4 airfoils with no LE stall tendency. This is done through the use of moderate camber to transfer part of the adverse pressure gradient from

the LE to a more aft position where the jet will help the flow to stay attached. Cambered pitching airfoil generally suffer from larger nose-down moment peak compared to their symmetric counterpart which makes their use problematic [18]. However implementing CFJ on cambered airfoils is effective to smoothen the moment coefficient. This means CFJ can be implemented on high performance cambered airfoil without being penalized by the nose-down moment. To ensure a reasonable injection jet exit velocity and reduce the jet exit shock structures, the injection slot size is doubled compared to previous study [19]. The suction slot size is also doubled. Finally the suction slot is moved upstream to 60% chord in order to increase the mass flow withdrawn at large AoA. The injection location is kept very close to LE to effectively remove dynamic stall. All airfoils have the same thickness of 9.5% chord to be consistent with the SC1095 airfoil.

Four airfoils are created as the iteration process to improve the performance. The first airfoil, namely Design 1, has a thick rounded LE to give space for the injection cavity and a very upstream injection slot location to prevent LE separation. A small camber is used to prevent LE separation at large AoA and increase the aerodynamic performance. The Design 2 and Design 3 (CFJ-NACA1209 and CFJ-NACA2209b)CFJ airfoils are implemented based on a NACA1209 and a NACA2209. Those airfoils feature a moderate camber of 1.6% respectively 2.4%. The Design 4 CFJ airfoil (CFJ-NACA2209b) is identical to the CFJ-NACA2209a airfoil, at the exception of the injection and suction cavity. The redesigned suction cavity avoid the internal flow separation. The redesigned injection cavity features a slightly higher and more uniform jet exit pressure. The airfoils and cavities geometries are shown and compared Fig. 3.

2.5 Pitching Conditions

The Mach number is 0.4 and Reynolds number is 5.24×10^6. To compare with the pitching motion of the SC1095 airfoil tested in [5] at Mach 0.3, the same pitching motion is used as:

$$AoA = \alpha_0 + \alpha_1 \, sin(k\,t)$$

where the mean angle α_0 is 10°, the reduced frequency k is 0.1 and the variable oscillation amplitude, α_1, can have three distinct values. The pitching motion is referred as motion 1 when $\alpha_1 = 5^\circ$, motion 2 when $\alpha_1 = 7.5^\circ$ and motion 3 when $\alpha_1 = 10^\circ$. For the CFJ airfoil, the C_μ used in this study is in the range of $0.08 - 0.14$ for the Design1, CFJ-NACA1209 and CFJ-NACA2209a airfoils and in the range $0.05 - 0.08$ for the CFJ-NACA2209b with reduced power consumption due to improved injection and suction cavity design.

3 Results

Due to the absence of experimental data available at M=0.4, the simulation validation is done at M=0.3 for the SC1095 airfoil. A good agreement is obtained between the computation and the experiment [19]. Also a mesh and time step refinement study are performed for numerous computation cases and very good agreement have been found with the baseline results. All of these validations have laid a good foundation for the numerical simulations below.

3.1 Design 1 Airfoil

The Design 1 baseline and CFJ airfoils flow fields are shown in Figs. 4 and 5 during motion 1. The thick LE generates a strong adverse pressure gradient that triggers an early separation at $AoA \approx 11.5^\circ$ on the baseline airfoil as seen in Fig. **??**. The CFJ airfoil increases the LE flow acceleration and the flow becomes choked at upstream of the injection slot. The flow is also shocked at the injection slot and supersonic downstream of the slot as displayed on Fig. 5. The choked injection flow limits the injection

energy added to the mainflow and the pitching airfoil still has a large separation that is difficult to remove.

3.2 The Design 2 (CFJ-NACA1209) and Design 3(CFJ-NACA2209a) Airfoil

The Design 3 NACA2209 baseline airfoil flow field is seen in Fig. 6 during motion 1. The flow field appears to be more attached than in the Design 1. When implementing CFJ, the LE acceleration is contained during motion 1 and a weak shock wave appears at the airfoil LE. The shock intensity increases during motion 2 and 3. The dynamic stall is either removed or largely mitigated for each C_μ and motion studied as seen on Figs. 7 and 8. lift, drag and moment amplitude are significantly improved over the baseline airfoil. The time averaged forces and moment shown in Fig. 9 confirm this trend for the 3 motions studied. The L/D_{ave} value reaches 50.7 for motion 1 at $C_\mu = 0.14$ while the moment amplitude is reduced by a factor of 10 in the same conditions. The unsteady shock-BL interaction increases ΔCm during motion 3 at high C_μ.

The Design 2 CFJ-NACA1209 CFJ airfoil has similar performance as the CFJ-NACA2209a although the time average lift and L/D are slightly lower due to the lower camber. The moment is similar between the two airfoils suggesting that CFJ can be implemented on highly cambered pitching airfoils without suffering from the large nose-down moment peak typically associated with highly cambered pitching airfoils.

3.3 CFJ-NACA2209b Airfoil

The CFJ-NACA2209b airfoil is generated to lower the power consumption by removing the suction cavity recirculation and injecting a jet with a slightly higher and more uniform pressure. The C_μ is lowered to the range $0.05 - 0.08$ to further reduce the power consumption.

The CFJ2209b airfoil flow field is shown Fig .10 for motion 1 at $C_\mu = 0.06$. The flow remains attached during most of the pitching motion. A small recirculation located between the suction slot and the TE of the airfoil appears between $AoA = 13.9°$ pitching up and $AoA = 13.9°$ pitching down. Overall losses due to this recirculation are limited as seen Fig.7. At high AoA, a shock wave structure appear just upstream the injection slot. There is virtually no jet exit shock structures as seen in previous designs. This is due to the redesigned injection cavity as well as to the reduced C_μ. In addition there is virtually no suction cavity recirculation.

Fig. 7, and 8 show a radical improvement in lift, drag and moment for all motions and $C_\mu \geq 0.06$. The $C_\mu = 0.05$ jet is not capable of reattaching the flow downstream the LE shock which leads to lower performance than with the baseline profile that exhibit no LE shock. No high frequency oscillation is found which indicate that the redesigned injection cavity and the lower C_μ used in this study successfully removed the unsteady shock-BL phenomena. The dynamic stall is removed for motion 1 and largely mitigated for motion 2 and motion 3.

The forces and moment time average values seen in Fig. **??** show a performance improvement for all motions and C_μ studied at the exception of the motion 1 at $C_\mu = 0.05$. The power consumption remains contained. With no unsteady shock-BL phenomena, the moment variation is greatly reduced in a monotonic manner. When comparing the CFJ-NACA2209b to the CFJ-NACA2209a airfoil, during motion 1 at $C_\mu = 0.08$, the time average L/D is improved by 2% and reaches 34.6 while the power consumption is lowered by 29% to a modest 0.74. Those achievements suggest that the injection and suction cavity design are of up-most importance for the power consumption of a given CFJ airfoil. The best performance improvement for the energy consumption is achieved at $C_\mu = 0.06$. During motion 1, a C_μ reduction from 0.08 to 0.06 lower the time average L/D by only 15% and the power consumption by 40%.

4 Conclusions

Pitching airfoils with Co-Flow Jet (CFJ) flow control are simulated using a high order URANS solver at Mach number 0.4 with reduced frequency of 0.1. The flow is transonic with shock wave boundary layer interaction. The airfoil oscillate around its mean angle of attack (AoA) of 10° with amplitude of 5°, 7.5° and 10° respectively. The study demonstrates that the CFJ pitching airfoil is very effective to remove dynamic stall at high Mach number of 0.4. The performance is significantly enhanced with radically increased lift, reduced drag, and decreased moment variation. The study indicates that the internal cavity design with no separation is crucial to minimize the CFJ power consumption.

References

[1] William G. Bousman, "Airfoil Dynamic Stall and Rotorcraft Maneuverability." NASA/TM 2000-209601, AFDD/TR 00-A-008, 2000.

[2] W.J. McCroskey, L.W. Carr, and K.W. McAlister, "Dynamic Stall Experiments on Oscillating Airfoils." U.S. Army Air Mobility RnD Laboratory, Moffett Field, Calif., 1975.

[3] Prouty, R. W., "The Whys and Whats of Pitch-Link Loads." Rotor and Wing International, vol.22, no.10, 1988, pp 17-19.

[4] W.J. McCroskey, "Unsteady Airfoils." Fluid Mechanics, vol.14, 1982, pp 285-311.

[5] K. W. McAlister, S. L. Pucci, W. J. McCroskey and L. W. Carr, "An Experimental Study of Dynamic Stall on Advanced Airfoil Sections Volume 1. Summary of the Experiment." NASA TM 84245, 1982.

[6] K. W. McAlister and C. Tung, "Suppression of Dynamic Stall with a Leading-Edge Slat on a VR-7 Airfoil." NASA Technical Paper 3357, 1993.

[7] Asitav Mishra, "A Coupled CFD/CSD Investigation of the Effects of Leading Edge Slat on Rotor Performance." University of Maryland, Ph.D. thesis, 2012.

[8] Kwanjung Yee, Wandon Joo, and Dong-Ho Lee, "Aerodynamic Performance Analysis of a Gurney Flap for Rotorcraft Application." Journal of Aircraft, May, Vol. 44, No. 3 : pp. 1003-1014, 2007.

[9] D. Thakkar, R. Ganguli, "Single-crystal piezoceramic actuation for dynamic stall suppression." Sensors and Actuators, Volume 128, Issue 1, 2006.

[10] M. Sun, S. R. Sheikh, "Dynamic stall suppression on an oscillating airfoil by steady and unsteady tangential blowing." Aerospace Science and Technology, Volume 3, Issue 6, 1999.

[11] G.-C. Zha, W. Gao, and C. Paxton, "Jet Effects on Co-Flow Jet Airfoil Performance," *AIAA Journal, No. 6,*, vol. 45, pp. 1222–1231, 2007.

[12] G.-C. Zha and D. C. Paxton, "A Novel Flow Control Method for Airfoil Performance Enhancement Using Co-Flow Jet." *Applications of Circulation Control Technologies*, Chapter 10, p. 293-314, Vol. 214, Progress in Astronautics and Aeronautics, AIAA Book Series, Editors: Joslin, R. D. and Jones, G.S., 2006.

[13] G.-C. Zha, C. Paxton, A. Conley, A. Wells, and B. Carroll, "Effect of Injection Slot Size on High Performance Co-Flow Jet Airfoil," *AIAA Journal of Aircraft*, vol. 43, 2006.

[14] G.-C. Zha, B. Carroll, C. Paxton, A. Conley, and A. Wells, "High Performance Airfoil with Co-Flow Jet Flow Control," *AIAA Journal*, vol. 45, 2007.

[15] Wang, B.-Y. and Haddoukessouni, B. and Levy, J. and Zha, G.-C., "Numerical Investigations of Injection Slot Size Effect on the Performance of Co-Flow Jet Airfoil," *Journal of Aircraft*, vol. 45, No. 6, pp. 2084–2091, 2008,.

[16] B. P. E. Dano, D. Kirk, and G.-C. Zha, "Experimental Investigation of Jet Mixing Mechanism of Co- Flow Jet Airfoil." AIAA-2010-4421, 5th AIAA Flow Control Conference, Chicago, IL, 28 Jun - 1 Jul 2010.

[17] B. P. E. Dano, G.-C. Zha, and M. Castillo, "Experimental Study of Co-Flow Jet Airfoil Performance Enhancement Using Micro Discreet Jets." AIAA Paper 2011-0941, 49th AIAA Aerospace Sciences Meeting, Orlando, FL, 4-7 January 2011.

[18] J. Watkinson, *The art of the helicopter*. Elsevier Butterworth-Heinemann, 2004.

[19] A. Lefebvre, G-C. Zha, "Numerical Simulation of Pitching Airfoil Performance Enhancement Using Co-Flow Jet Flow Control," June 2013.

[20] P. Spalart and S. Allmaras, "A One-equation Turbulence Model for Aerodynamic Flows." AIAA-92-0439, 1992.

[21] Y.-Q. Shen and G.-C. Zha, "Large Eddy Simulation Using a New Set of Sixth Order Schemes for Compressible Viscous Terms ," *Journal of Computational Physics*, vol. 229, pp. 8296–8312, 2010.

[22] G.-C. Zha, Y. Shen, and B. Wang, "An improved low diffusion E-CUSP upwind scheme ," *Journal of Computer & Fluids*, vol. 48, pp. 214–220, 2011.

[23] Y.-Q. Shen and G.-Z. Zha , "Generalized finite compact difference scheme for shock/complex flowfield interaction," *Journal of Computational Physics*, vol. doi:10.1016/j.jcp.2011.01.039, 2011.

[24] Shen, Y.-Q. and Zha, G.-C. and Wang, B.-Y., " Improvement of Stability and Accuracy of Implicit WENO Scheme," *AIAA Journal*, vol. 47, No. 2, pp. 331–344, 2009.

[25] Y.-Q. Shen, G.-C. Zha, and B.-Y. Wang, "Improvement of Stability and Accuracy of Implicit WENO Scheme ," *AIAA Journal*, vol. 47, pp. 331–344, 2009.

[26] Shen, Y.-Q. and Zha, G.-C. and Chen, X.-Y., " High Order Conservative Differencing for Viscous Terms and the Application to Vortex-Induced Vibration Flows," *Journal of Computational Physics*, vol. 228(2), pp. 8283–8300, 2009.

[27] Shen, Y.-Q. and Zha, G.-C. , " Improvement of the WENO Scheme Smoothness Estimator," *International Journal for Numerical Methods in Fluids*, vol. DOI:10.1002/fld.2186, 2009.

[28] G.-C. Zha and E. Bilgen, "Numerical Study of Three-Dimensional Transonic Flows Using Unfactored Upwind-Relaxation Sweeping Algorithm," *Journal of Computational Physics*, vol. 125, pp. 425–433, 1996.

[29] B.-Y. Wang and G.-C. Zha, "A General Sub-Domain Boundary Mapping Procedure For Structured Grid CFD Parallel Computation," *AIAA Journal of Aerospace Computing, Information, and Communication*, vol. 5, No.11, pp. 2084–2091, 2008.

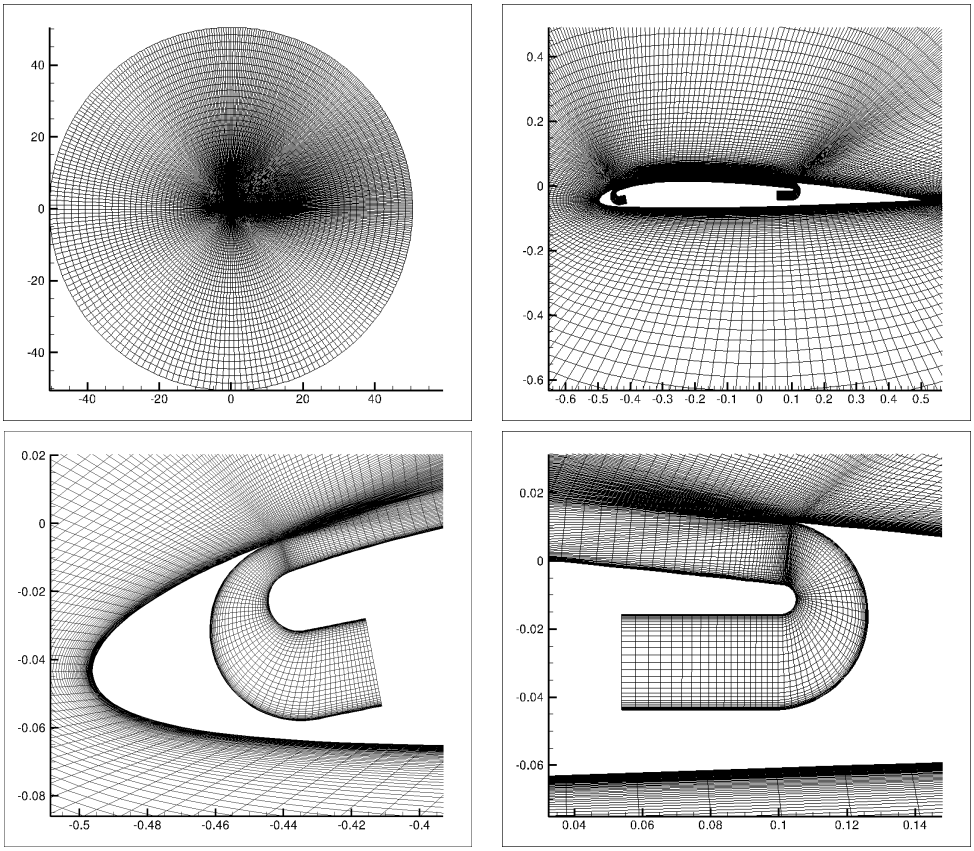

Figure 2: CFJ-NACA2209 CFJ pitching airfoil mesh topology. Similar mesh is applied to the other airfoils.

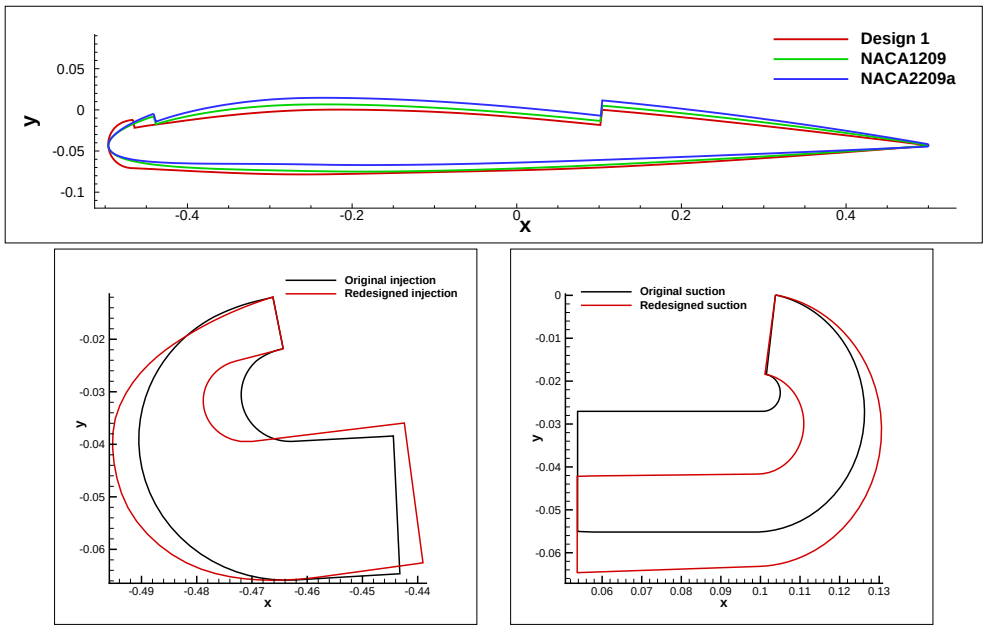

Figure 3: Airfoils and cavities geometry comparison.

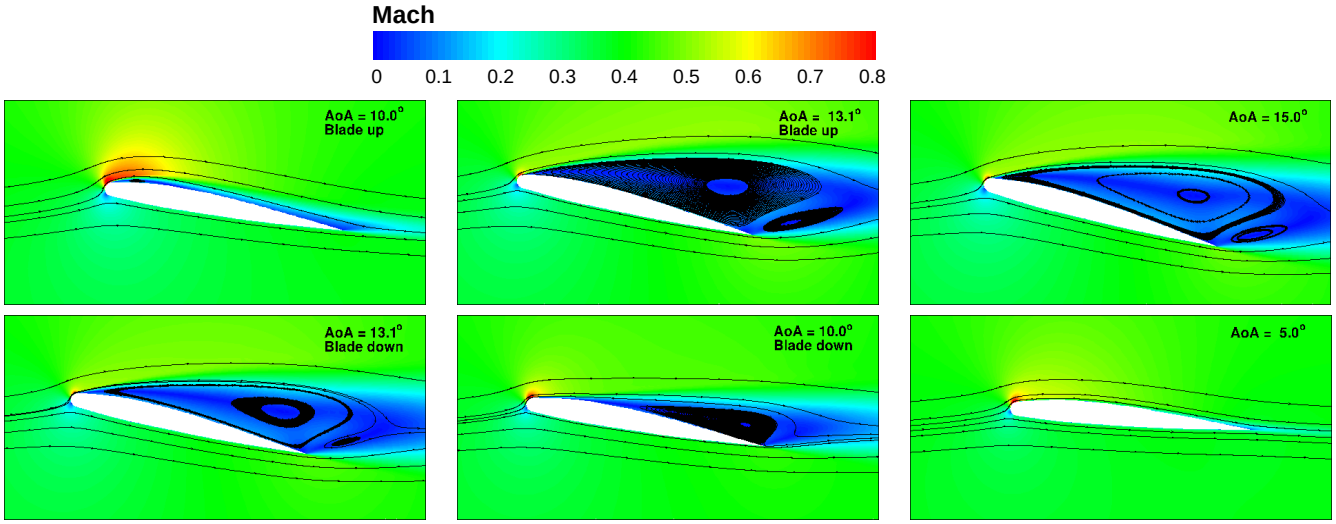

Figure 4: Instantaneous Mach contour of the baseline design1 pitching airfoil with streamlines at different AoA during motion 1.

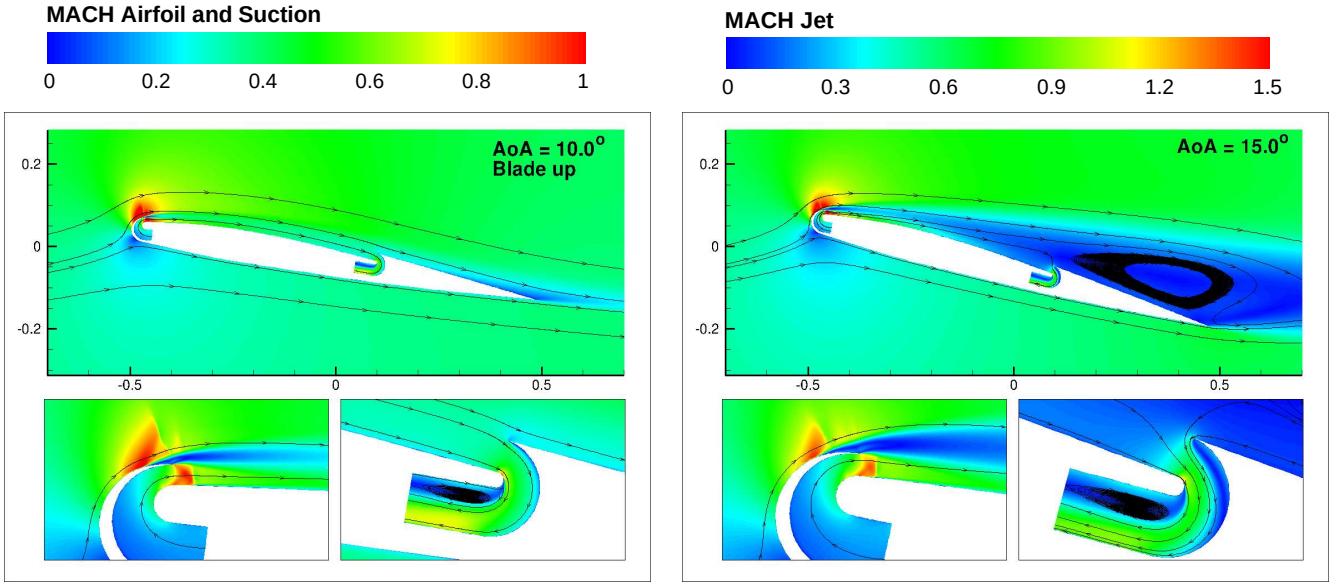

Figure 5: Instantaneous Mach contour of the CFJ Design 1 pitching airfoil at $C_\mu = 0.08$ with streamlines at different AoA during motion 1.

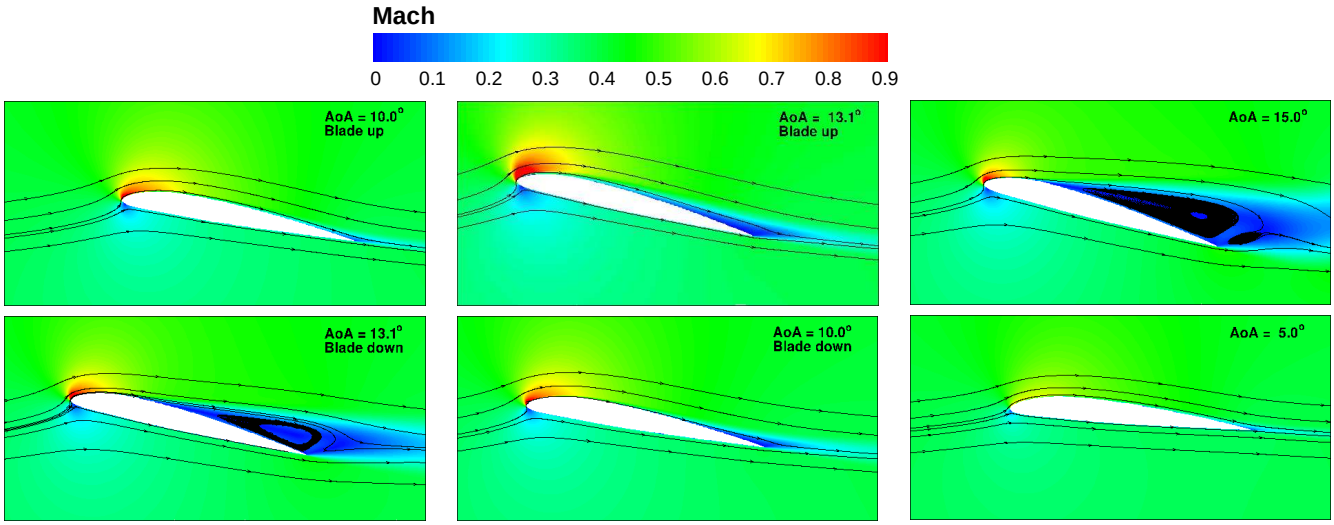

Figure 6: Instantaneous Mach contour of the baseline NACA2209 pitching airfoil with streamlines at different AoA during motion 1.

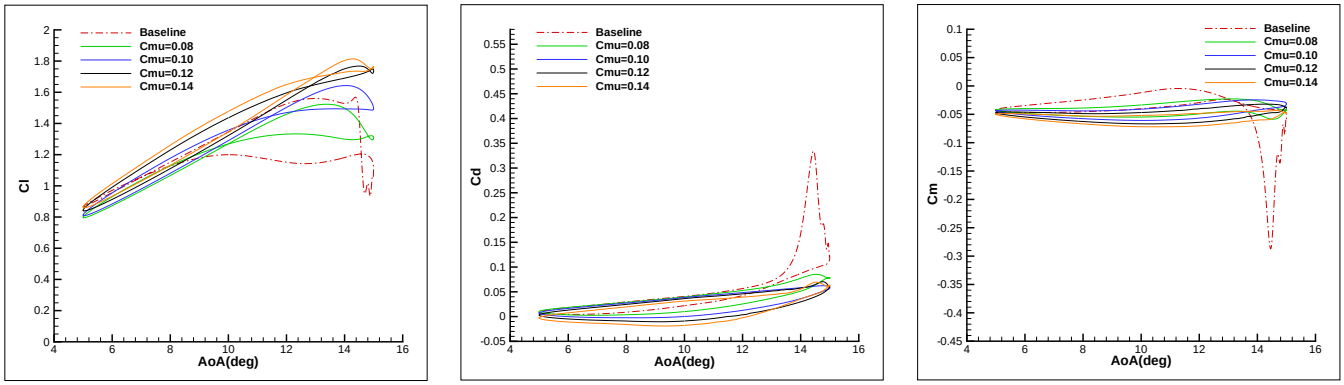

Figure 7: NACA2209 baseline pitching airfoil C_l, C_d and C_m compared with CFJ-NACA2209a data during motion 1.

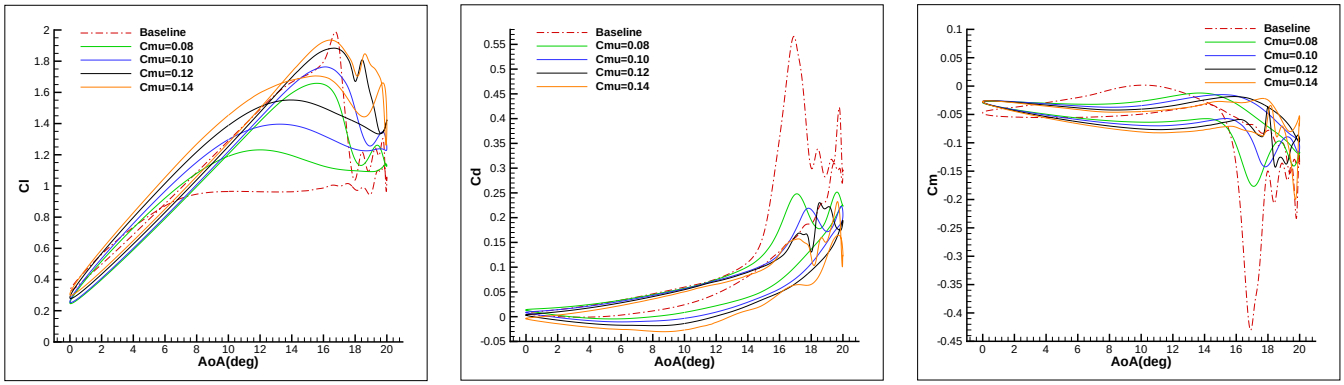

Figure 8: NACA2209 baseline pitching airfoil C_l, C_d and C_m compared with CFJ-NACA2209a data during motion 3.

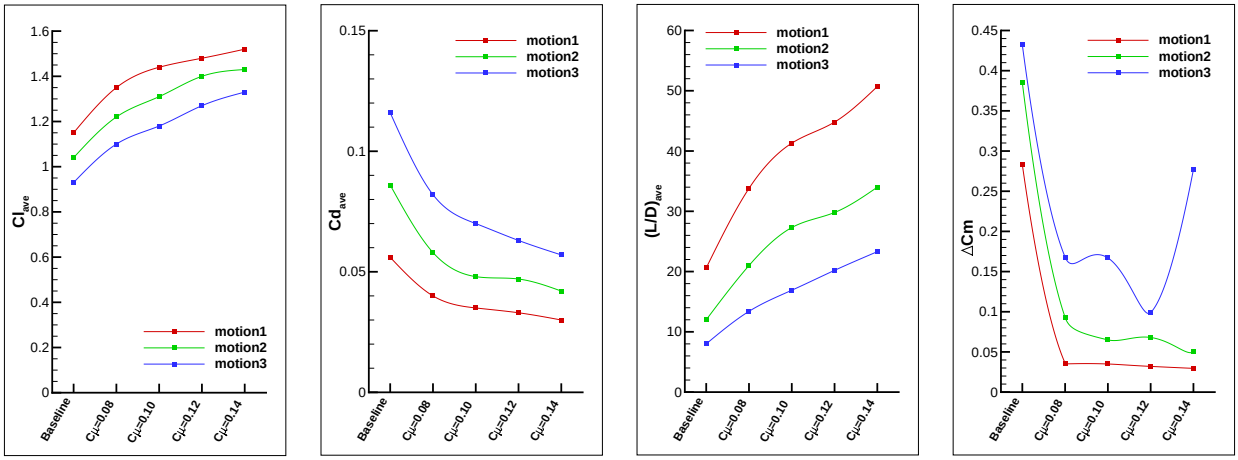

Figure 9: Time average performance of the NACA2209 baseline and CFJ-NACA2209a airfoil.

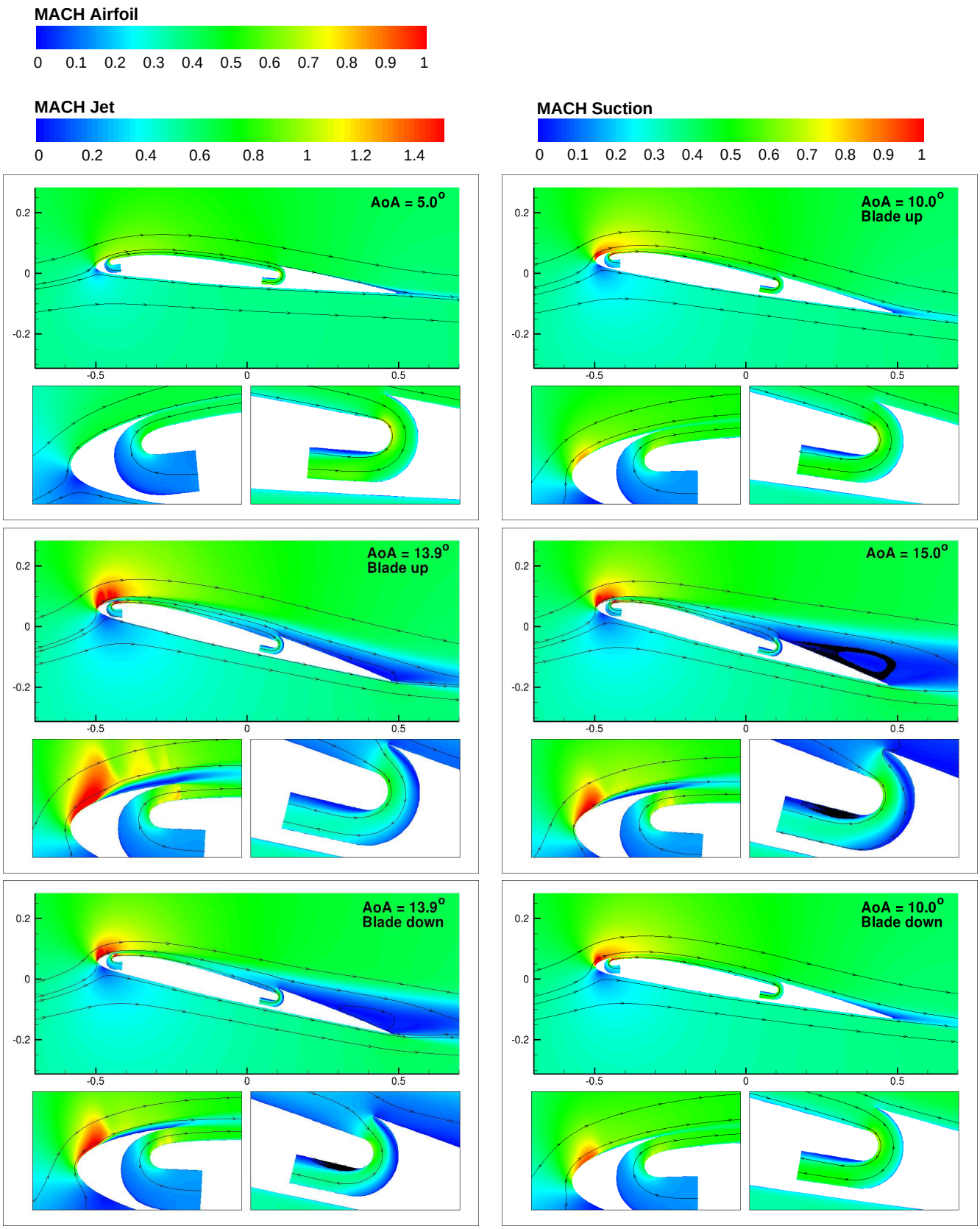

Figure 10: Instantaneous Mach contour of the CFJ-NACA2209b pitching airfoil at $C_\mu = 0.06$ with streamlines at different AoA during motion 1.

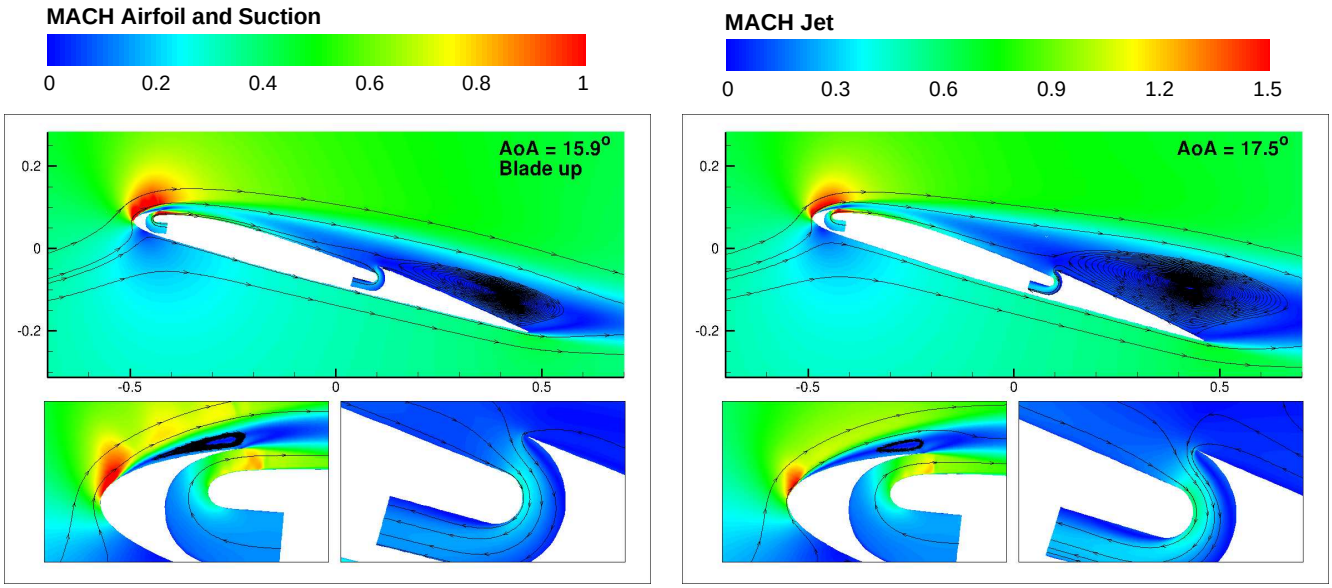

Figure 11: Instantaneous Mach contour of the CFJ-NACA2209b pitching airfoil at $C_\mu = 0.08$ with streamlines at different AoA during motion 2.

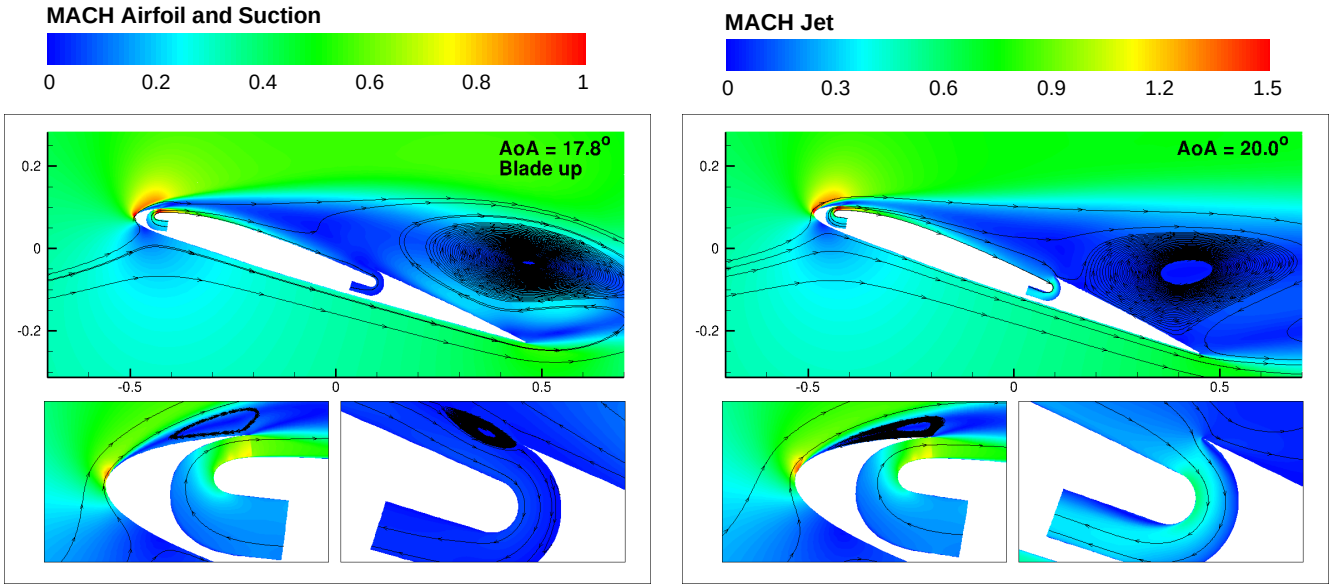

Figure 12: Instantaneous Mach contour of the CFJ-NACA2209b pitching airfoil at $C_\mu = 0.08$ with streamlines at different AoA during motion 3.

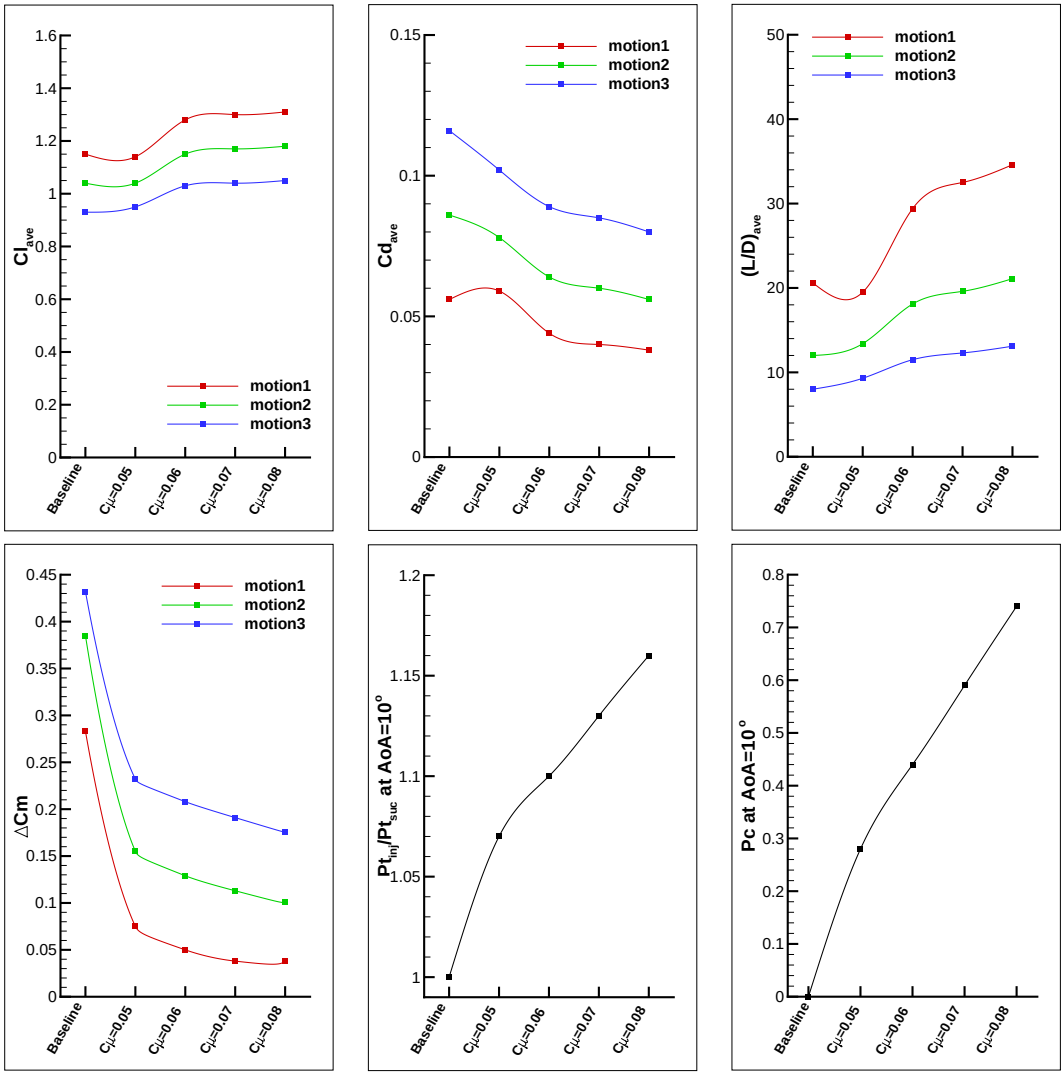

Figure 13: Time average performance of the CFJ-NACA2209 baseline and CFJ2209b airfoil.

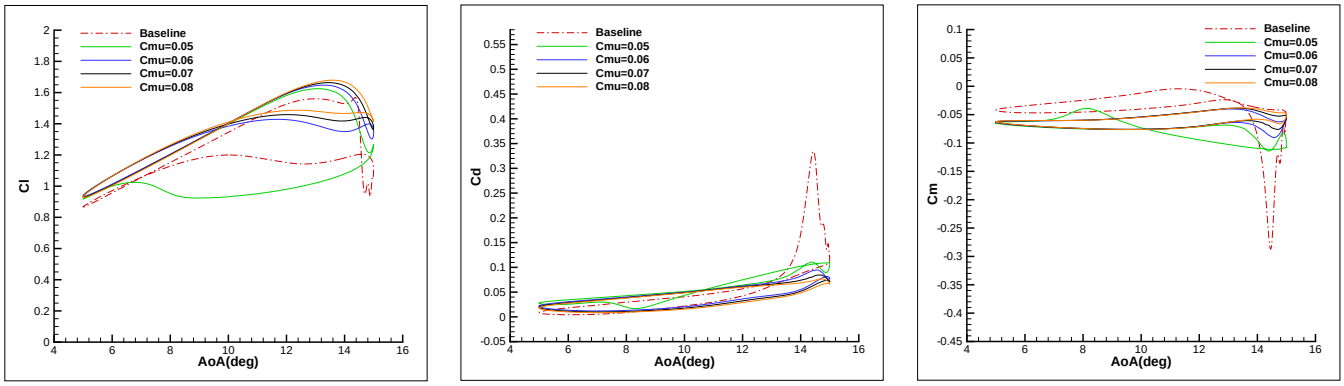

Figure 14: NACA2209 baseline pitching airfoil C_l, C_d and C_m compared with CFJ-NACA2209b data during motion 1.

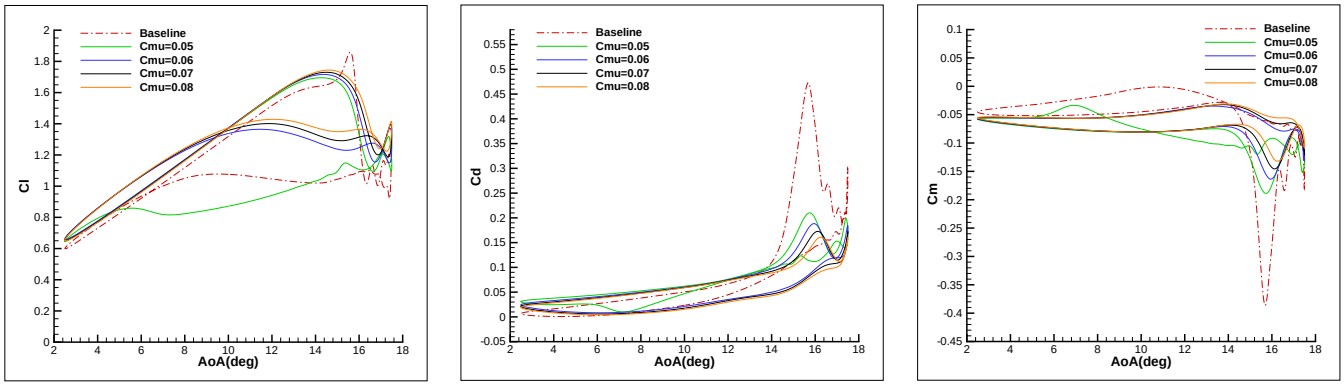

Figure 15: NACA2209 baseline pitching airfoil C_l, C_d and C_m compared with CFJ-NACA2209b data during motion 2.

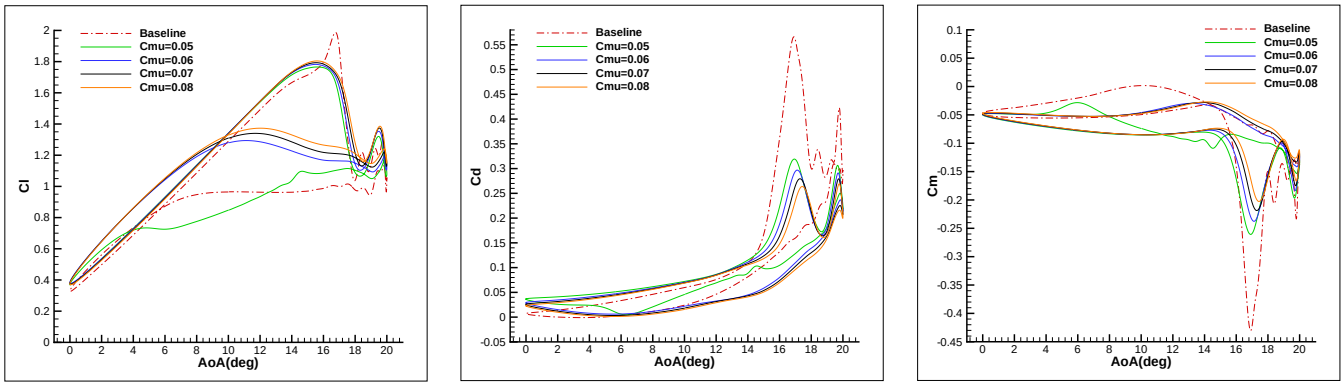

Figure 16: NACA2209 baseline pitching airfoil C_l, C_d and C_m compared with CFJ-NACA2209b data during motion 3.